Electronic Supplementary Information: Data-Driven Stabilization of Ni_mPd_{n-m} Nanoalloys: A Study Using Density Functional Theory and Data Mining Approaches

Tiago M. Souza,*,† Lucas B. Pena,*,† Juarez L. F. Da Silva,*,‡ and Breno R. L. Galvão*,†,¶

†*Centro Federal de Educação Tecnológica de Minas Gerais, CEFET-MG, Av. Amazonas* 5253, 30421-169, *Belo Horizonte, Minas Gerais, Brazil*

‡*São Carlos Institute of Chemistry, University of São Paulo, P.O. Box* 780, 13560-970, *São Carlos, SP, Brazil*

¶*Department of Chemistry and Chemical Biology, University of New Mexico, Albuquerque, 87131, New Mexico, USA.*

E-mail: tiagomendesdesouza75@gmail.com; lucas.bernardesp205@gmail.com; juarez_dasilva@iqsc.usp.br; brenogalvao@gmail.com

Contents

1 Details of the DFT Calculations

Table S1: Technical details of the PAW-PBE projectors selected for this study. Recommended cutoff energy for the plane-wave basis set, `ENMAX` (eV), number of valence electrons, `ZVAL`, and valence electronic configuration

Element	PAW projector	`ENMAX`	`ZVAL`	Valence Config.
Pd	Pd_sv_GW 05Dec2013	356.093	18	$4s^2 4p^6 4d^{10}$
Ni	Ni_sv_GW 05Dec2013	389.645	18	$3s^2 3p^6 3d^{10}$

2 Structure generation

2.1 Gupta Potential

The Gupta potential is expressed using the following equations.

$$E_i = E_i^{band} + E_i^{rep} \,, \tag{1}$$

where

$$E_i^{band} = -\left[\sum_{j\neq i}^{n} \xi^2 \exp\left\{\left[-2q\left(\frac{r_{ij}}{r^0}-1\right)\right]\right\}\right]^{\frac{1}{2}} \,, \tag{2}$$

and

$$E_i^{rep} = \sum_{j\neq i}^{n} A \exp\left\{\left[-p\left(\frac{r_{ij}}{r^0}-1\right)\right]\right\} \,. \tag{3}$$

E_i^{band} is the attractive part of the energy that accounts for the band character of the metals, and E_i^{rep} is the pairwise repulsion term. The parameters r_{ij} are the distance between the atoms i and j, while r^0 is the distance between the closest neighbors of the bulk phase.[1] The parameters ξ, p, q and A for the interaction pairs Ni–Ni and Pd–Pd are taken from Refs. 2,3 and are gathered in Table S2.

Table S2: Parameters of the empirical Gupta potential for Ni–Ni[2] and Pd–Pd interactions.[3]

Parameter	Ni–Ni	Pd–Pd
r^0 (Å)	2.491	2.749
A (eV)	0.038	0.175
ξ (eV)	1.070	1.718
p	16.999	10.867
q	1.189	3.742

2.2 Generation of Alloys

As discussed in the main manuscript, we have used in this work a protocol recently developed,[4?–10] that is summarized in Figures S1, S2, and S3. As can be seen, the first step is to optimize the unary cluster structures, from which we select the most stable unary structures for Ni and Pd, hereafter named parent structures. For the generation of alloy structures,

all possible permutations of the clusters are included if this number is less than 3000 (applicable to the clusters of 13 atoms and compositions Ni_3Pd_{24} and $Ni_{24}Pd_3$). In addition to these cases, 2.7×10^5 completely random permutations and other 1.3×10^5 design principles-based permutations were generated for each parent for the clusters with 27 atoms, while for the 41 atom size, the corresponding numbers are 3×10^5 random and 2×10^5 design-based. The Python scripts for the generation of random structures and design principles can be downloaded from the respective papers.[10]?

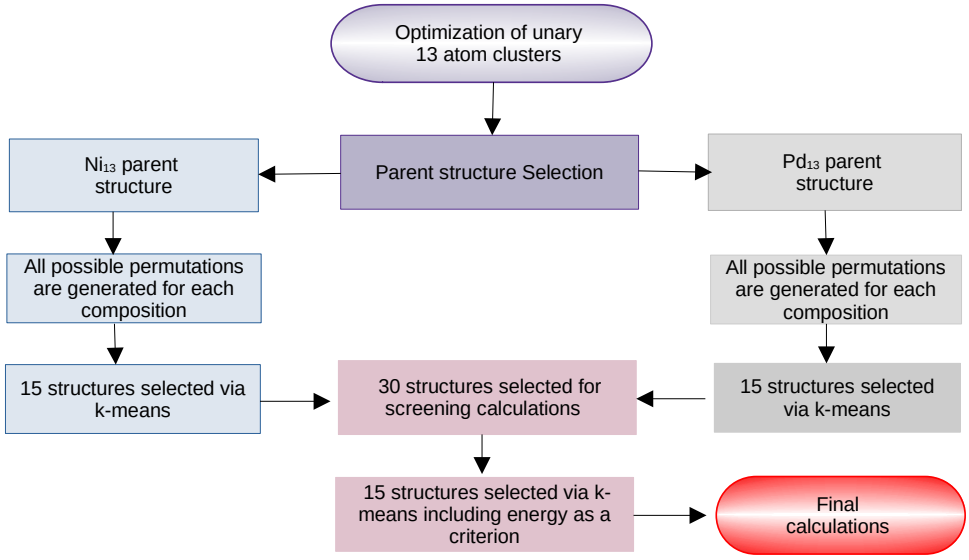

Figure S1: Flowchart for the 13 atoms alloys generation.

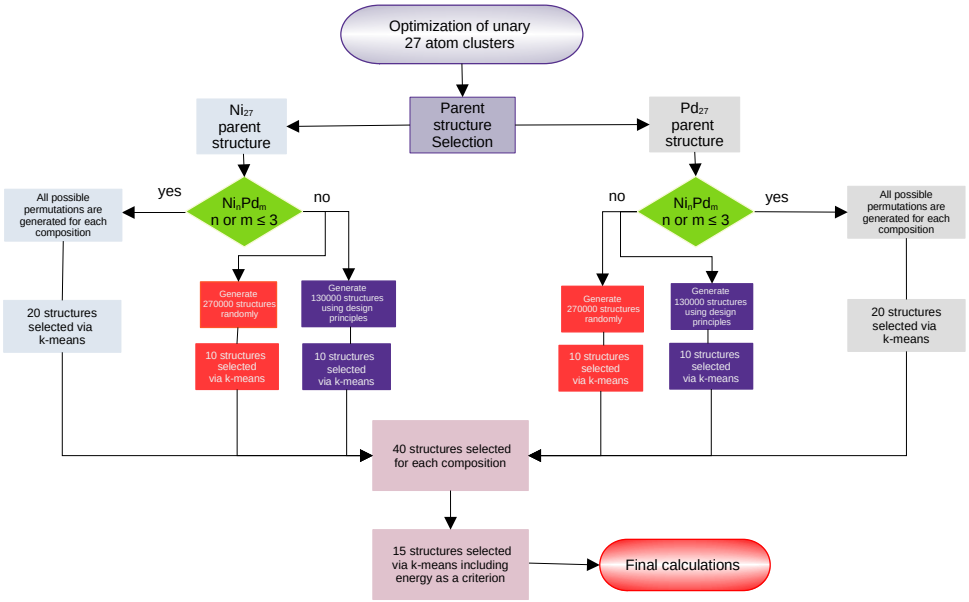

Figure S2: Flowchart for the 27 atoms alloys generation.

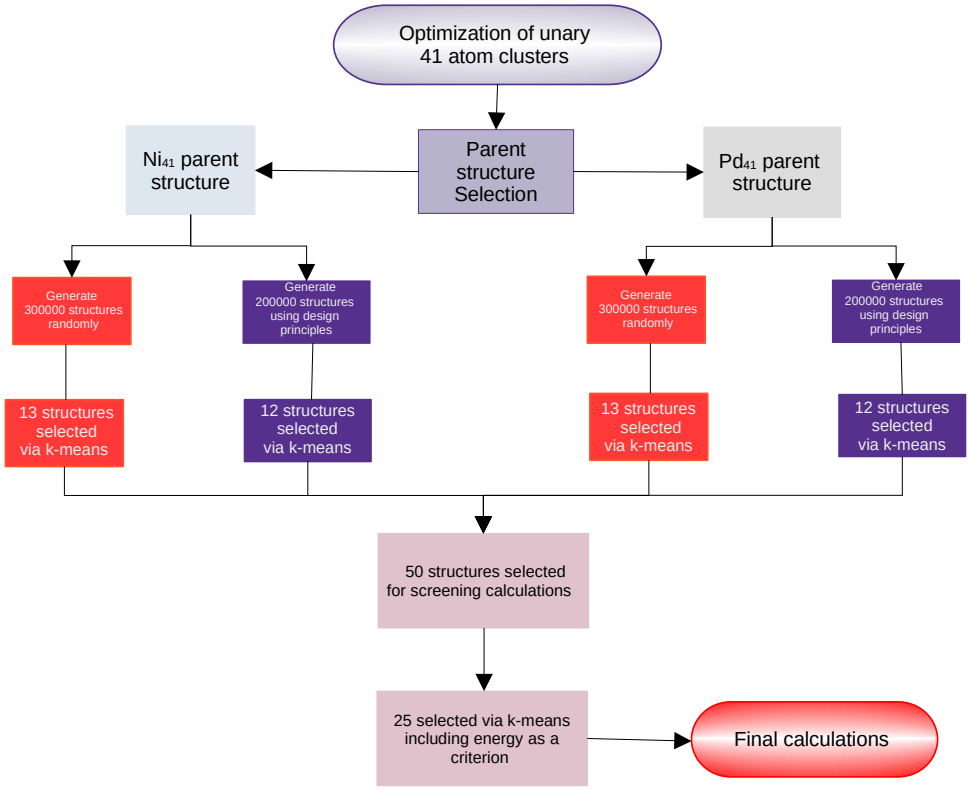

Figure S3: Flowchart for the 41 atoms alloys generation.

Given the large number of structures generated above, it is not possible to perform DFT calculations on all of them. Here, we employ machine learning techniques for reducing the number of screening and final calculations. For this, we use the Coulomb matrix (CM) representation[11] to change the Cartesian coordinates of the clusters $3N$ to the N eigenvalues of the CM matrix. The dimensionality is reduced further to two using the t-distributed neighborhood (t-SNE) method[11] The k-means method is then applied to select representative structures for each alloy among the sample space of generated structures. In this way, there is a reduction in computational costs with DFT calculations for each composition, while maintaining a structurally diverse set of coordinates for correlation analysis.[10]

2.2.1 k-means clustering

The k-means method is an important tool for clustering large databases, dividing them into new data subsets based on similarities between points. These new sets are called clusters, and their geometric center, known as the centroid, is the most representative point for each cluster. To define the similarity between the data (structure), we need to supply predetermined parameters

that allow differentiation between the points. At the beginning of the process, we provide the number (k) of clusters into which the algorithm will group the data. As the algorithm runs, the centroid position of each cluster changes, improving the distribution of data in this group. When the execution is completed, we have the most representative k groups from the data, from which each centroid is selected.[12]

2.2.2 Coulomb Matrix

For describing each structure for the k-means clustering algorithm, we employ the Coulomb matrix (CM). This matrix describes the repulsion between atoms I and J in the structure,[10,11] and its elements M_{IJ} are obtained as follows:

$$M_{IJ} = \begin{cases} 0.5 Z_I^{2.4} & \forall\, I = J, \\ \frac{Z_I Z_J}{|R_I - R_J|} & \forall\, I \neq J. \end{cases} \tag{4}$$

Here R_I is the Cartesian coordinate of the atom I and its nuclear charge Z_I. The nuclear repulsion energy between pairs of I and J is captured by the off-diagonal elements, while diagonal items encode a polynomial fit to the potential energy of the isolated atoms.[11] This representation does not change with respect to rotations and translations of the entire rigid structure. The eigenvalues of this matrix yield a vector ε which is used to measure the similarity between two different structures as[10]

$$d\,(\varepsilon, \varepsilon') = \sqrt{\sum_i |\varepsilon_i - \varepsilon_i'|^2}. \tag{5}$$

Each trial structure is converted to a feature vector with the CM eigenvalues. Matrix diagonalization reduces computational costs despite the high number of atoms per structure and system.[10]

2.2.3 t-distributed Stochastic Neighbor Embedding

For further minimization of computational costs and to avoid problems that arise from high-dimensional data (since the CM set of eigenvalues has the same number of dimensions as atoms), we employ the Stochastic Neighbor Embedding, t-SNE, for reduction of dimensionality

of the CM feature vector to two dimensions.[10,13] The t-SNE method uses the Student statistic distribution to determine the similarity between pairs of points of sample space with many dimensions, providing the optimization of their position in a lower-dimensional representation so that this representation mirrors the original data.[13] By doing that, the t-SNE algorithm tends to keep similar points close together in two dimensions, in which the k-means algorithm will be applied for selecting structures.[10]

2.2.4 Selected Structures for DFT Calculations

As seen in Fig.S1, we use the k-means approach to choose representative structures 15 for each parent of the 13 atom alloys, totaling 30 calculations for each composition, with the exception of $Ni_{12}Pd$ and $NiPd_{12}$ as these structures have only 13 possible permutations each. These structures are optimized at the screening DFT level.

For the 27 atoms clusters (Fig.S2) we select 10 random and 10 design-based permutations for each parent structure, except for Ni_3Pd_{24} and $Ni_{24}Pd_3$ wherein we employ a similar method that Ni_mPd_{13-m} systems to choose 20 structures for each parent, totaling 40. For clusters with 41 atoms, 13 random structures and 12 design-based ones for each parent were selected for the selection calculations, totaling 50.

After the DFT optimizations, we selected half of the structures using the same k-means method but with the calculated screening energy used to select the most stable structure per group (instead of the centroid). These are re-optimized at the final DFT level, and their properties are analyzed for the discussion.

3 Results for the Unary Clusters

3.1 Convergence Test with 13 Atoms Clusters

The convergence test is an important tool to choose the appropriate cut-off energies to address the screening calculations. From the convergence curves, an informed choice of the cutoff energy can be made.

3.1.1 13 atoms nickel cluster

In this paper, we use the geometries provided by Lu et al.[14] and Chaves et al.[15] to perform the Ni_{13} convergence test. The relative total energy of a structure x, ΔE^{x}_{tot}, is obtained as

$$\Delta E^{x}_{tot} = E^{x}_{tot} - E^{a}_{tot}, \tag{6}$$

where E^{x}_{tot} is its total energy and E^{a}_{tot} is the total energy of the lowest energy structure. The results are shown in Figures S4 and S5. Unlike predicted in previous works, the icosahedral geometry (labeled as geometry c) does not show the lowest energy.[16–20] Our results agree with the more recent work of Lu et al.,[14] where the truncated triangular bipyramid showed the lowest energy.

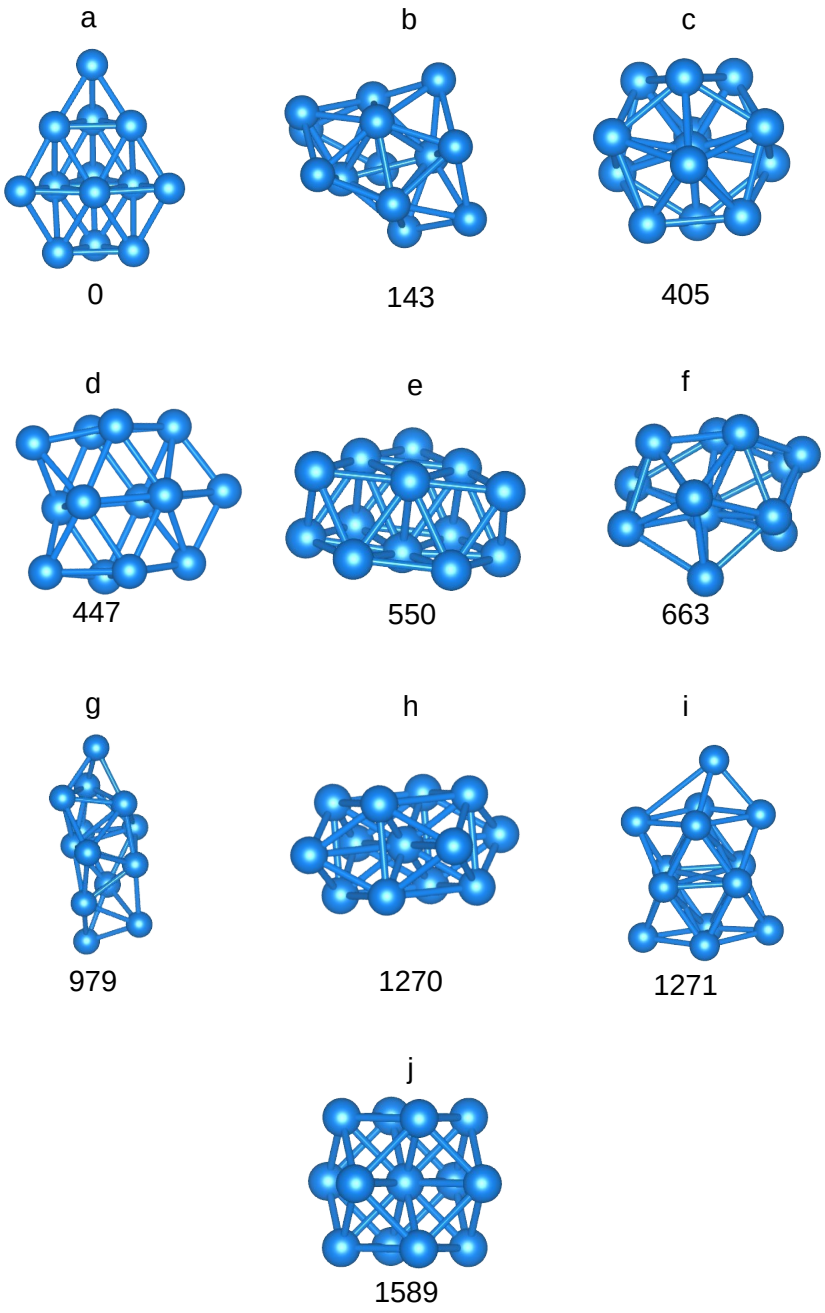

Figure S4: Selected structures and relative energies (in meV) for the 13-atoms nickel clusters available in literature [14,15] (with cutoff energy of 438.351 eV).

For the screening calculations, it is desirable that the calculations are accurate enough to obtain the correct order between the different isomers, while for the final calculations, we aim at converged results. Looking at Figure S5(b), we see that the energetic order among the different isomers changes when the cutoff energy changes from 292 to 340 eV, while remaining unchanged after this point. For this reason, we chose the 340.939 eV (12.5 % lower than the largest recommended value from the PAW projectors (`ENMAX`)) for the screening calculations.

For the final calculations, we use the value 438.351 eV for unary Ni clusters, which is 12.5 % larger than ENMAX, and can be seen to be converged.

3.1.2 13 atoms palladium cluster

For Pd_{13}, we use a geometry extracted from Chaves et al.[15] (labeled a), Blanco-Rey et al.[21] (labeled b) and others from Nava et al.[22] The structure with the lowest total energy is in agreement with Chaves et al.[15] as shown in Figures S6 and S7. Here again we did not find the icosahedral geometry to be energetically favored, as reported by Lopez et al.[23] working with small metal clusters, and reported by Sachdev et al.[24] for Pd_{13} clusters.

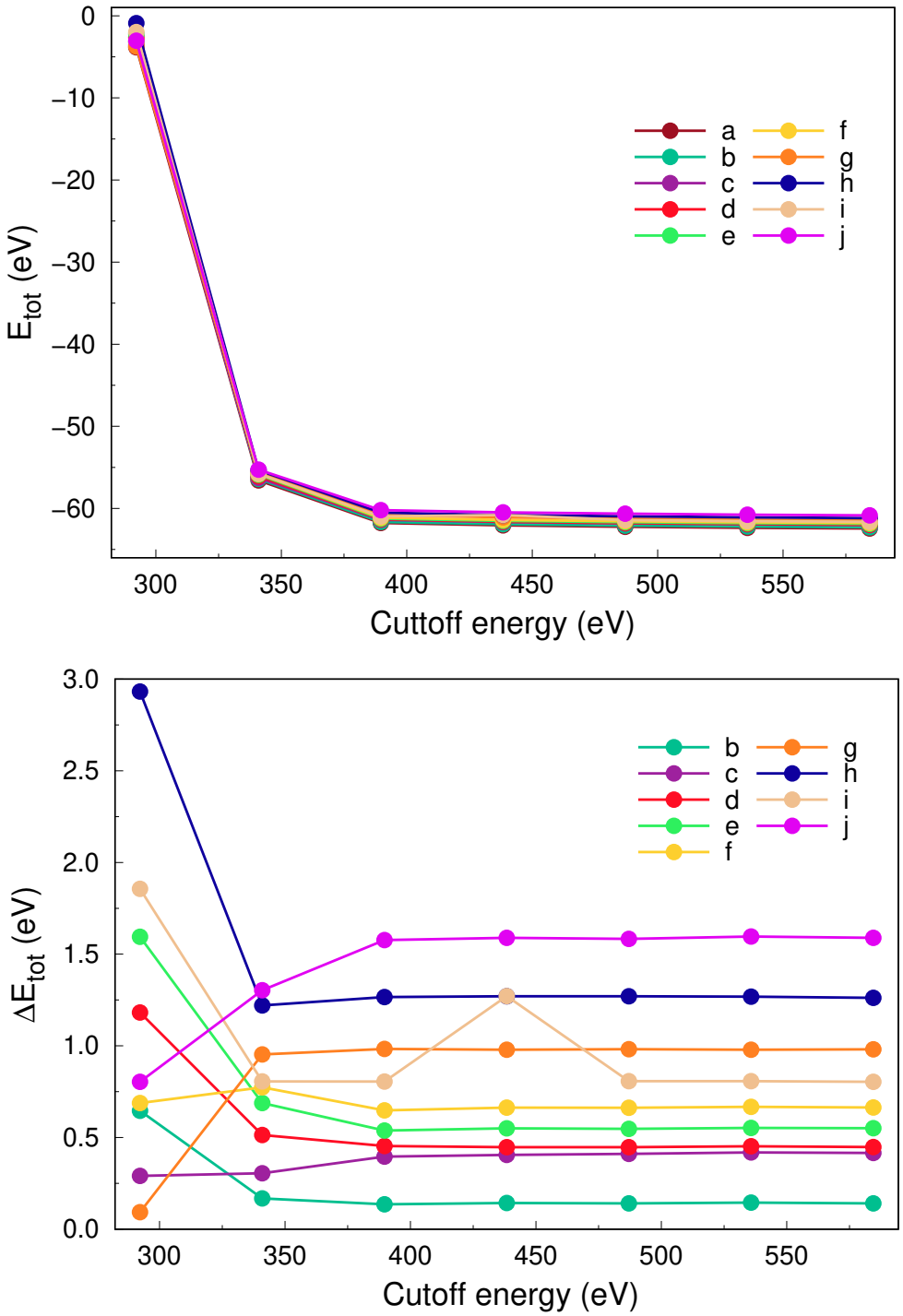

Figure S5: Total energy convergence with respect to cutoff energy and relative energies for Ni_{13} isomers.

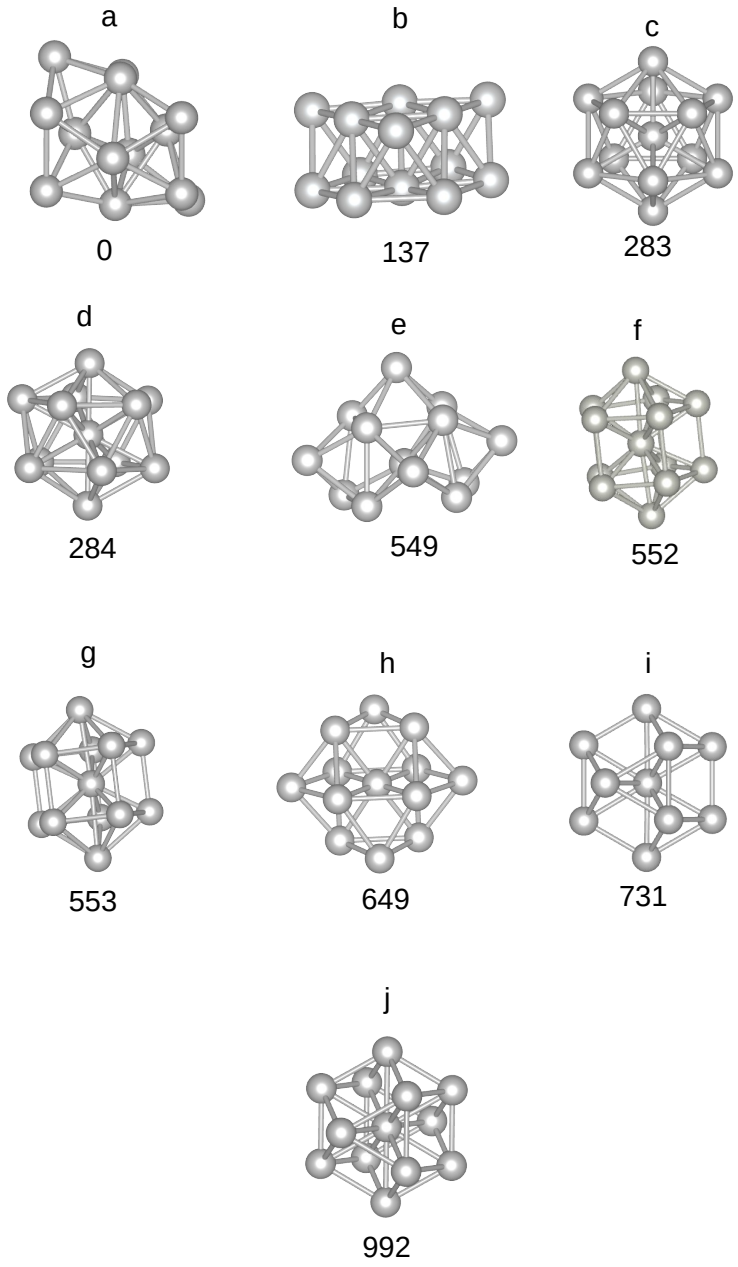

Figure S6: Selected structures and relative energies (meV) for the 13-atoms palladium clusters available in literature[15,21,22] cutoff energy of 400.605 eV).

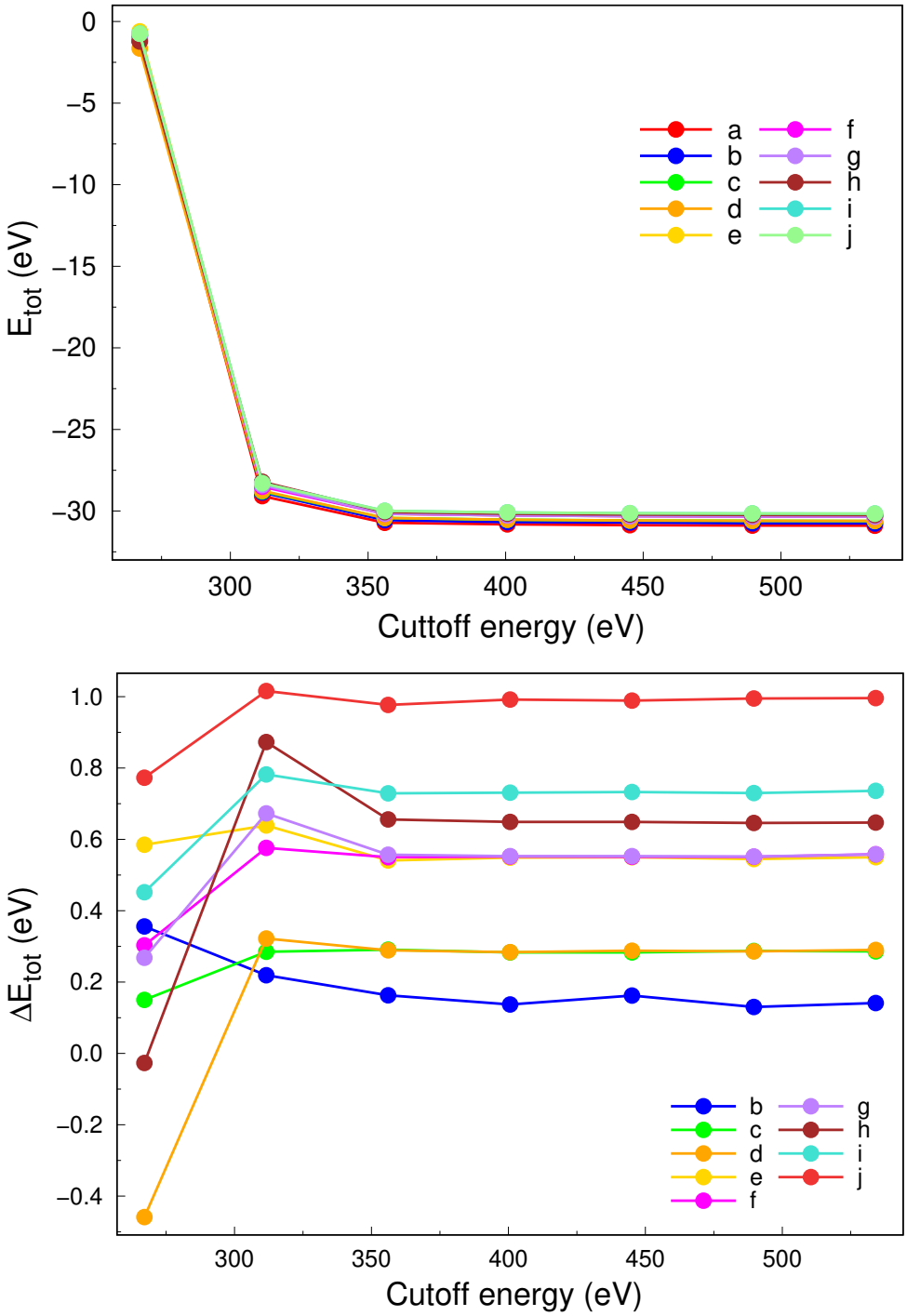

Figure S7: Total energy convergence with respect to cutoff energy and relative energies for Pd_{13} isomers.

Similarly to what was observed for the Ni_{13} clusters, with a cutoff energy 12.5 % lower than `ENMAX` (311.581 eV), the calculations already predict the structure (a) as the global minimum, and the order of relative energies is similar to that of the highest cutoff value. Once again,

we consider a cutoff 12.5 % larger than `ENMAX` to be convergent and sufficient for the final calculations.

3.2 Screening For Unary Clusters with $n = 27$ and 41

As described in the main manuscript, no detailed study was available in the literature on the geometries of unary clusters with 27 and 41 atoms, and for this reason, we used a genetic algorithm coupled with an empirical potential to yield many low-energy structures for optimization at the DFT level. The results for the screening stage are given in Figures S8 and S9, showing both the binding energies and the magnetic moment. It is seen that the empirical potential provided a set of structures with energetic diversity (as given by the screening DFT calculations.

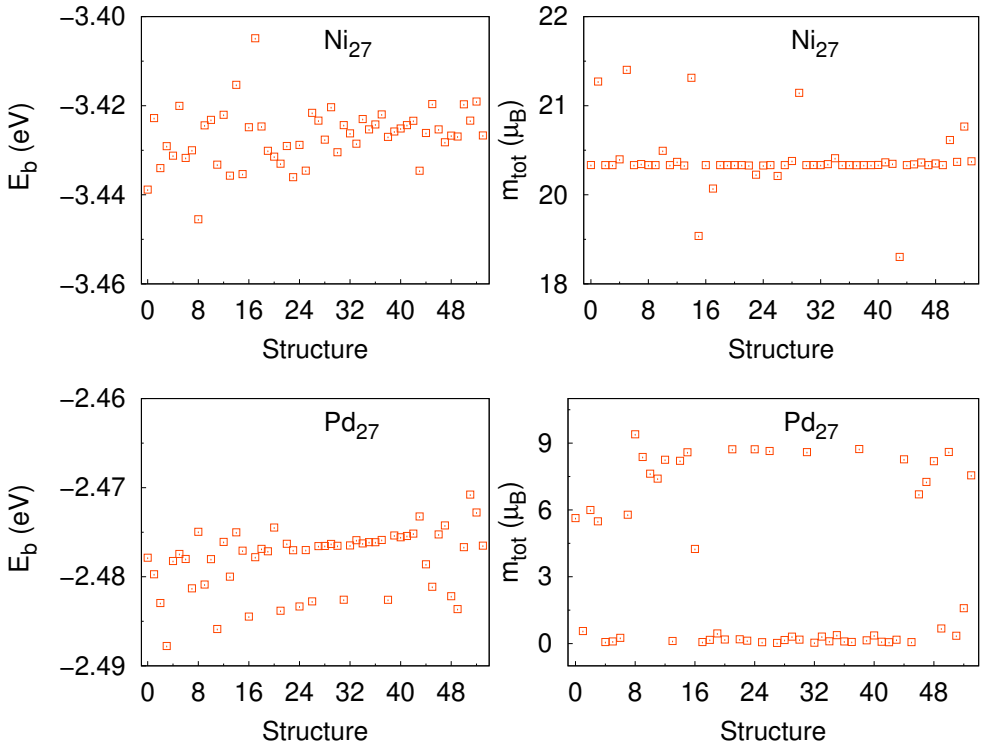

Figure S8: From top to bottom, binding energy per atom(E_b) and magnetic moment(m_{tot}) for Ni_{27}(above) and Pd_{27}(bellow) clusters at the screening DFT level.

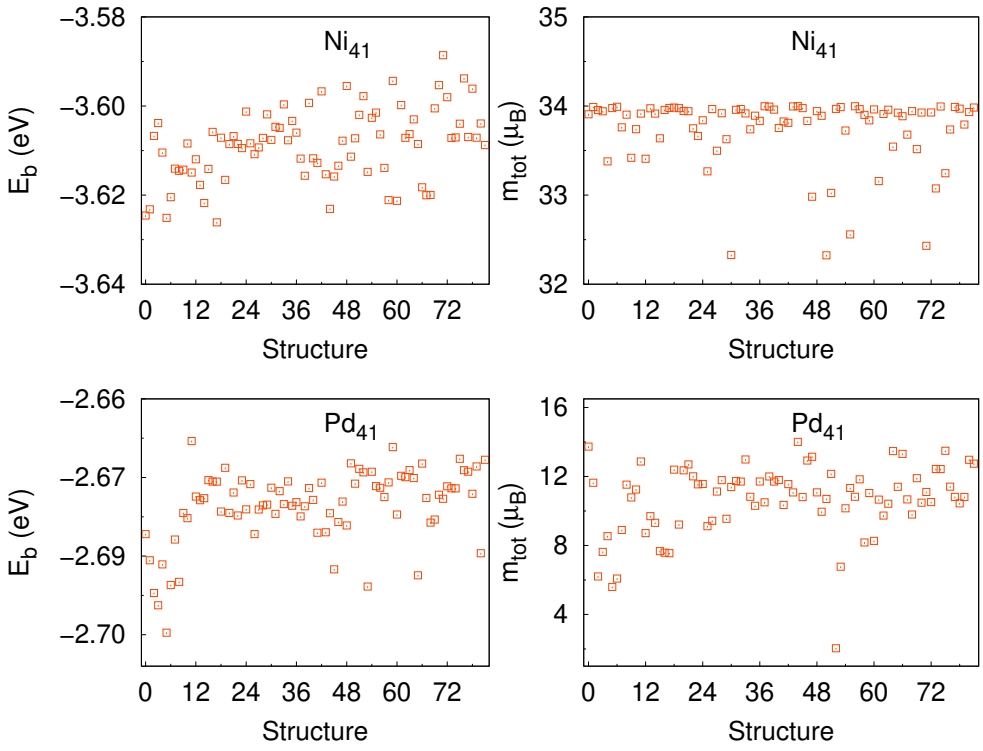

Figure S9: Binding energy per atom(E_b) and magnetic moment(m_{tot}) for Ni_{41}(above) and Pd_{41}(below) clusters at the screening DFT level.

The binding energy for Ni_{27} geometries are between -4.33 eV and -4.29 eV, similar to previous results.[19,25] For Pd_{27} structures the binding energies lie around -2.49 and -2.47 eV. The magnetic moment for most Ni_{27} isomers is concentrated around $20\mu_B$. The Pd_{27} isomers showed magnetic moments from 0 to $10\mu_B$.

We observed an increase in binding energies with the cluster size, as observed in previous works.[19,22,25,26] Here, the E_b for Ni_{41} lies between -4.52 and -4.46 eV, while for Pd_{41} between -2.70 to -2.67 eV. As observed for clusters with 27 atoms, different Ni clusters display similar magnetic moments, while for Pd a larger spread is observed.

3.3 Final Calculations For Unary Clusters

3.3.1 Final calculations for 27 atoms unary clusters

After re-optimizing the geometries with the more accurate final calculations for Ni_{27} and Pd_{27}, we obtained the structures given in Fig. S12. A selected set of properties is provided for all structures in Figures S10 and S11. We observe that most properties do not show a significant

correlation with relative energy (with the obvious exception E_b). These figures show that the empirical potential has provided us with a diverse set of structures instead of structures with similar geometric and energetic properties.

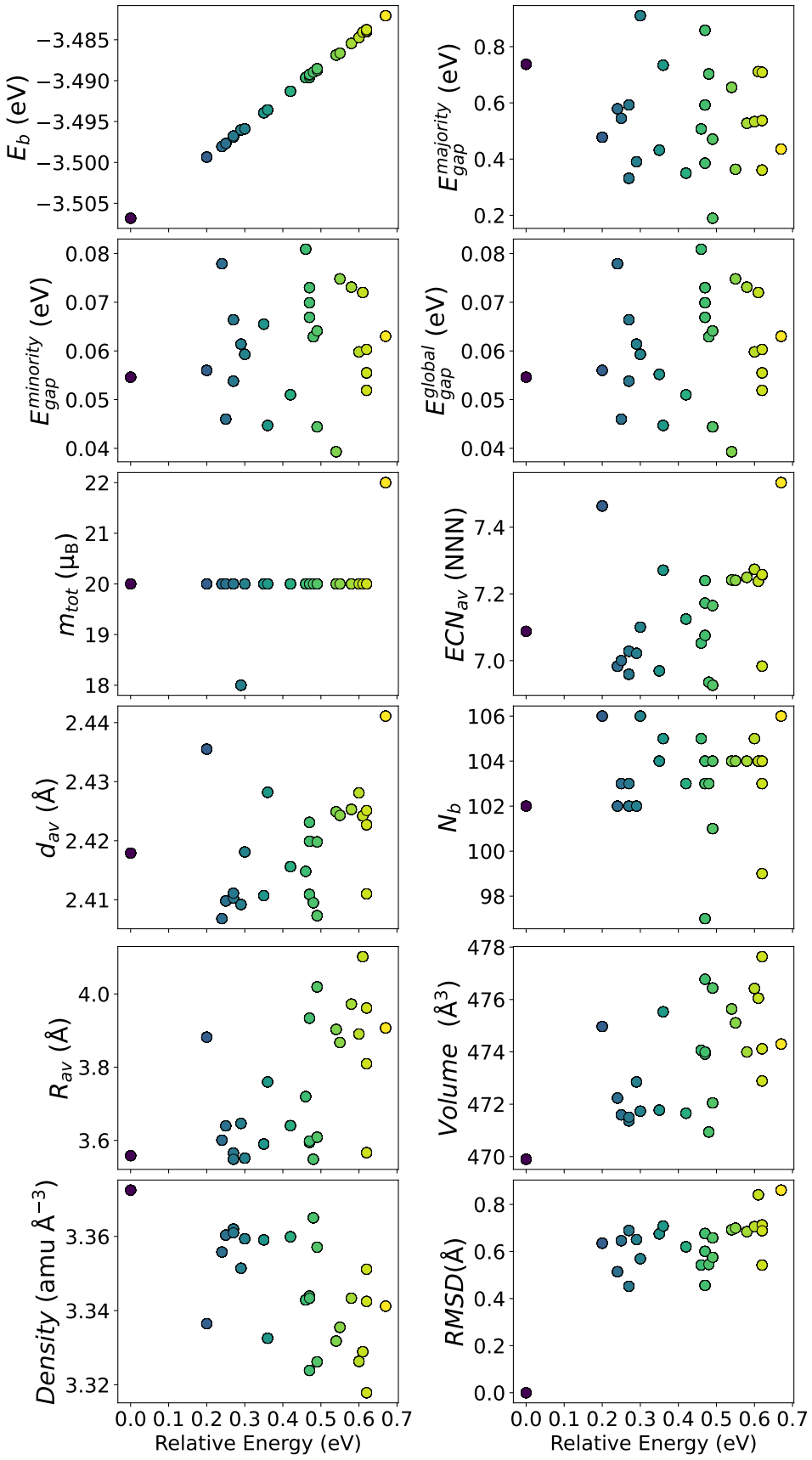

Figure S10: Electronic and structural properties of Ni_{27}. Lowest relative energies in dark blue, intermediary relative energies in green and largest ones in yellow.

Roughly, volume and density seem to have a small correlation with energy, with more compact structures presenting lower energy. Also worth highlighting is that the *RMSD* values show that none of the isomers can be considered geometrically similar to the lowest-energy ones.

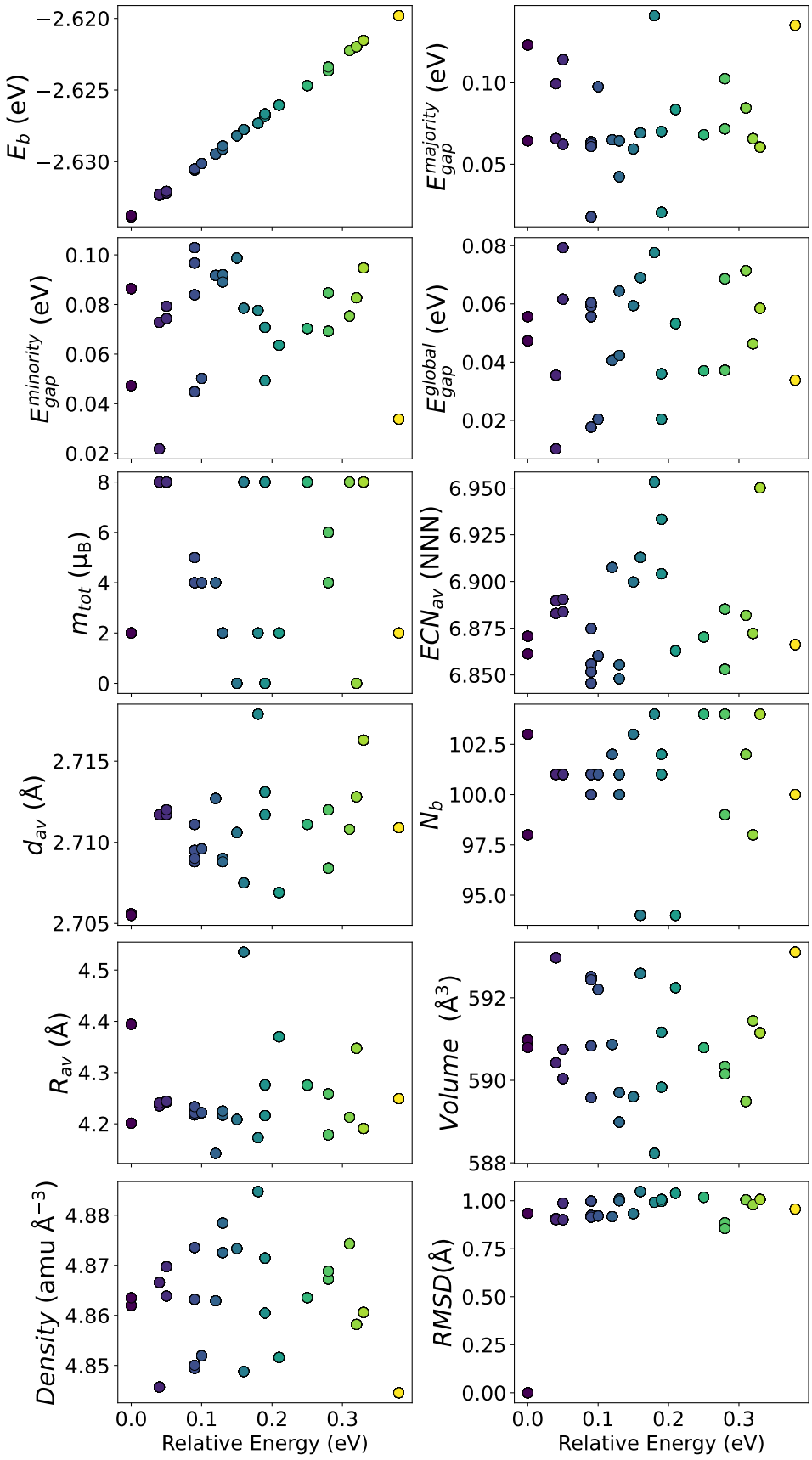

Figure S11: Electronic and structural properties of Pd_{27}. Lowest relative energies in dark blue, intermediary relative energies in green and largest ones in yellow.

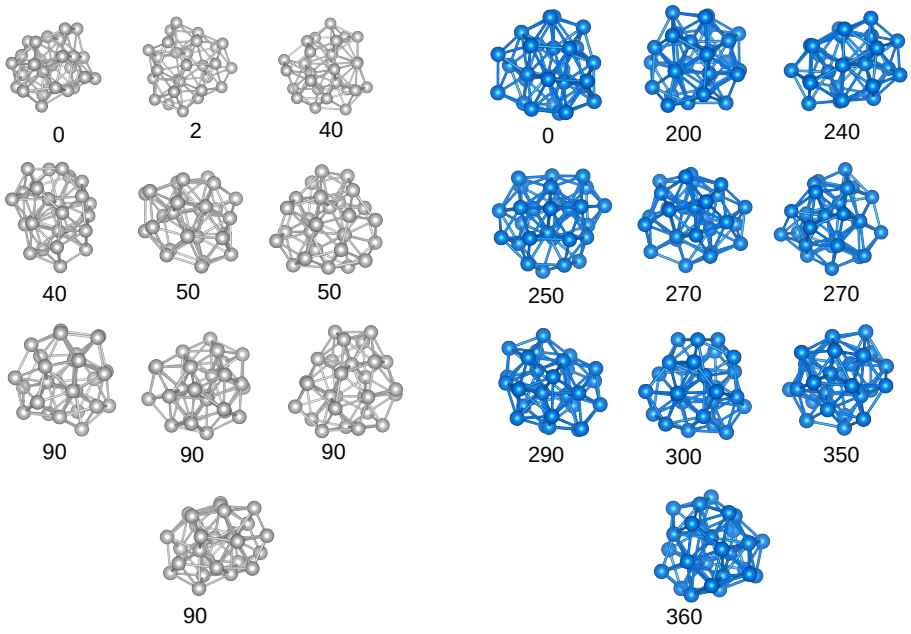

(a) Pd_{27}. (b) Ni_{27}.

Figure S12: ΔE_{tot}(meV) for the 10 geometries of 27-atom clusters with lowest energy for each atom.

3.3.2 Final calculations of 41 atoms unary clusters

After the final re-optimizations, the Ni_{41} and Pd_{41} structures obtained are shown in Figure S15. It is interesting to note that already at this cluster size, the Pd cluster presents itself as a bulk fragment, while the Ni cluster is more spheric-like. This is also observed for 55-atom clusters.[27]

As may be seen in Figures S13 and S14, the magnetic moment for the Pd_n clusters varies more than for the Ni_n clusters, for the sizes of the 27 and 41 clusters. Overall, the same trends observed for the 27 atom clusters for volume, density, and RMSD are seen for this cluster size.

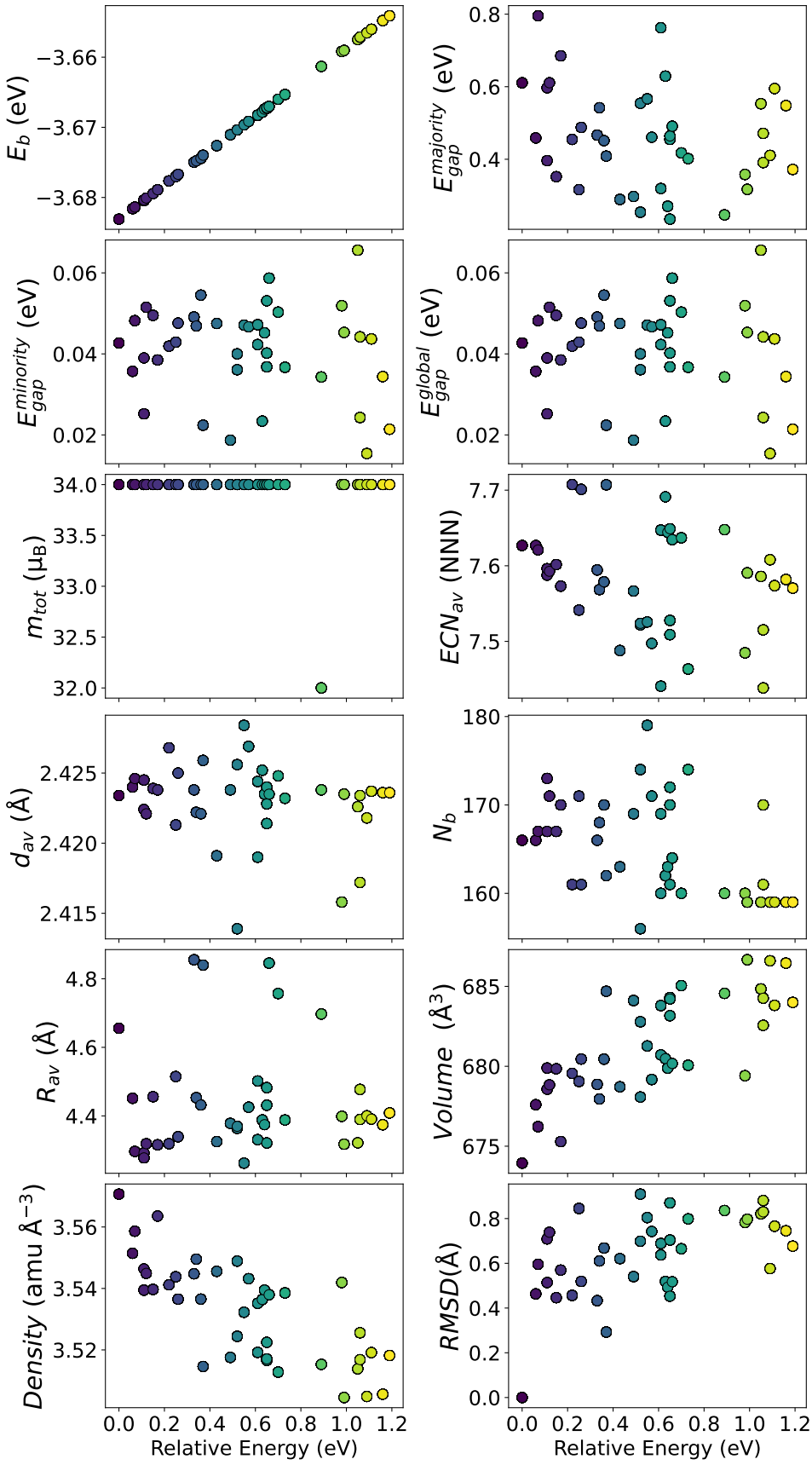

Figure S13: Electronic and structural properties of Ni_{41}. The lowest relative energies are shown in dark blue, the intermediary relative energies are shown in green, and the largest ones are shown in yellow.

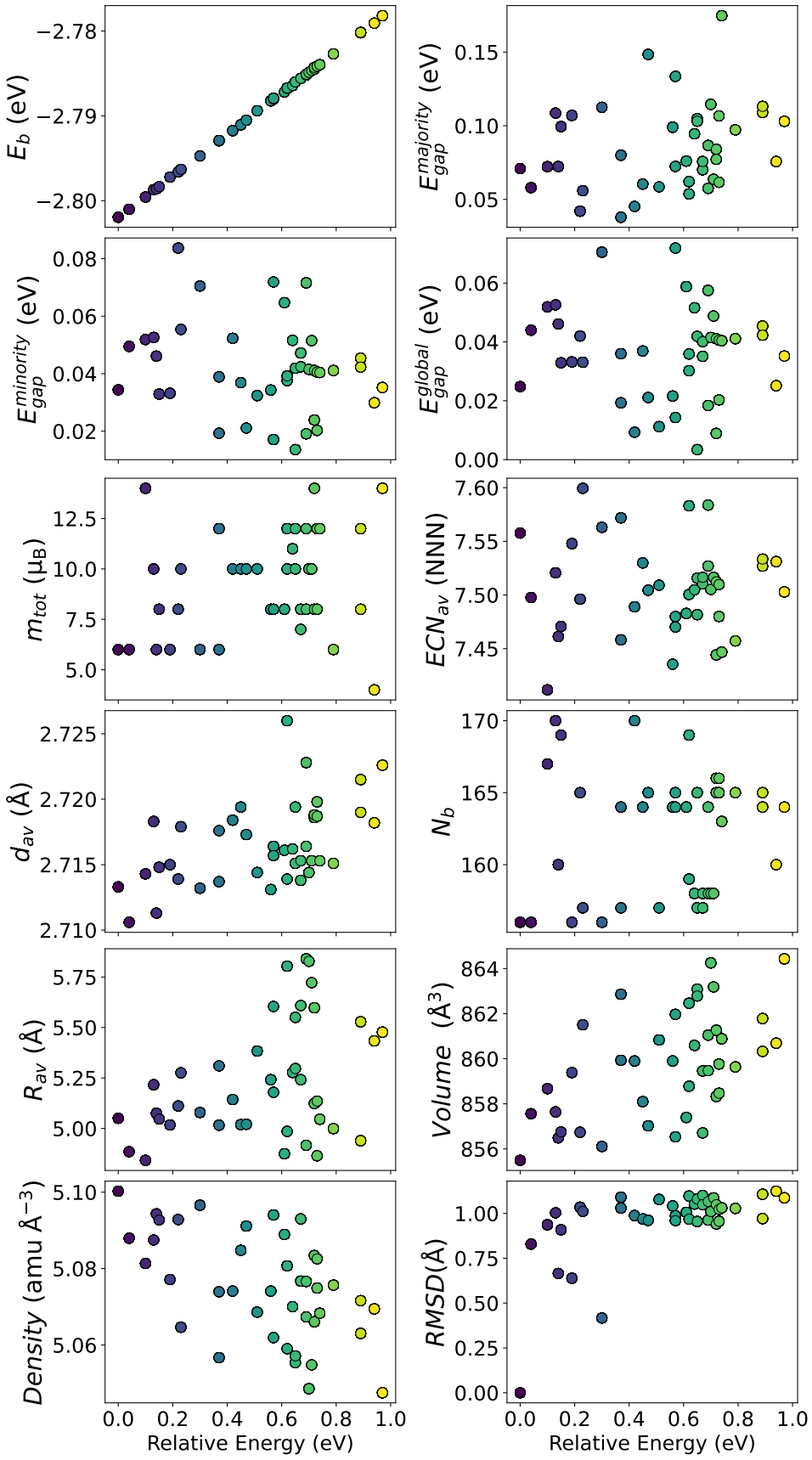

Figure S14: Electronic and structural properties of Pd_{41}. Lowest relative energies in dark blue, intermediary relative energies in green and largest ones in yellow.

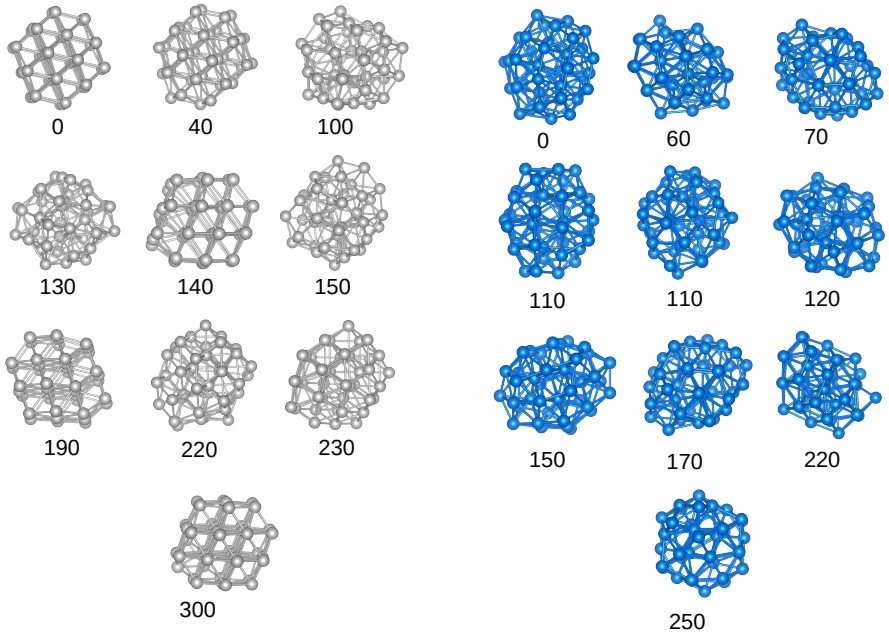

(a) Pd_{41}. (b) Ni_{41}.

Figure S15: ΔE_{tot}(meV) for the 10 geometries of 41-atom clusters with lowest energy for each atom.

4 Results for Alloys

4.1 Screening Calculation on NiPd Alloys

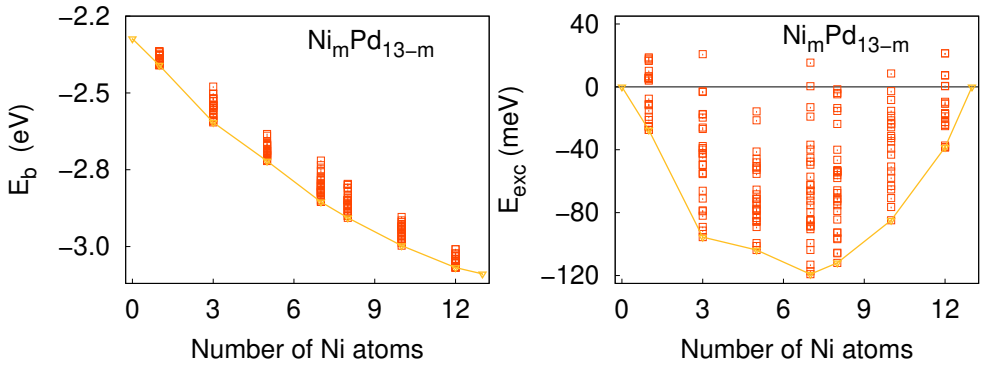

Figure S16: Binding and excess energies per atom of Ni_mPd_{13-m} alloys. The orange squares denotes the properties of each alloy and golden line describe the structures with lowest E_B and E_{exc}.

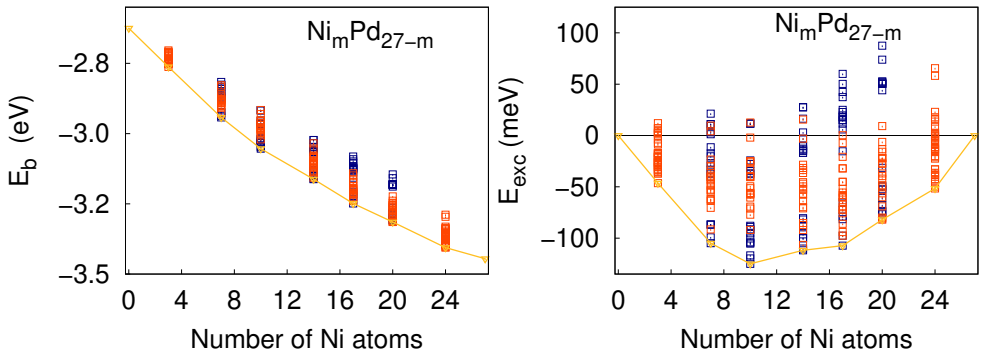

Figure S17: Binding and excess energies per atom of Ni_mPd_{27-m} alloys. Squares in orange denotes the geometries obtained by k-means with random permutations while blue squares depicts structures obtained by design principles. The golden line describe the structures with lowest E_B and E_{exc}.

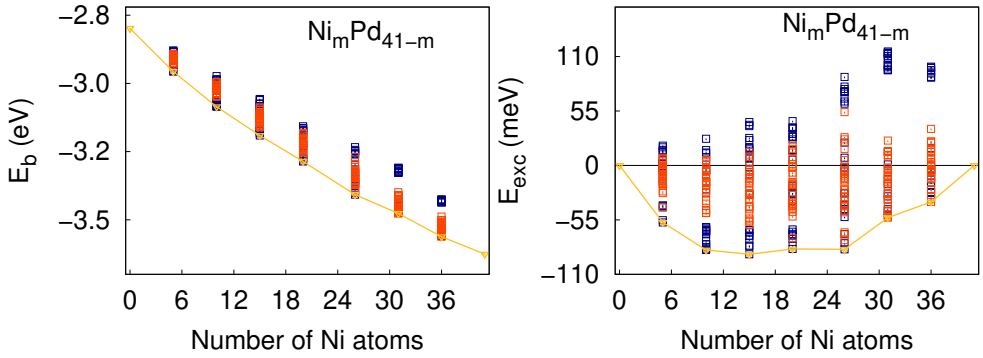

Figure S18: Binding and excess energies per atom of Ni_mPd_{41-m} alloys. Squares in orange denotes the randomly generated geometries while blue squares depicts structures obtained by design principles permutations. The golden line describe the structures with lowest E_B and E_{exc}.

4.2 Final calculations on NiPd Alloys

The figures in this section present the calculated electronic and structural properties for all structures at the final DFT level. This includes electronic properties not included in the main manuscript (such as $E_{gap}^{majority}$, $E_{gap}^{minorrity}$ and magnetic moments), as well as structural ones not included in the main text (such as the ECN and d_{av} specific for each element, number of bonds of each type, density, and others). As can be seen, the binding (E_b) and excess energies (E_{exc}) per atom calculated at the screening and final DFT levels show qualitative agreement, with E_b increasing in magnitude with the number of atoms, while E_{exc} decreasing in magnitude.

4.2.1 Final calculations on 13 atom NiPd alloys

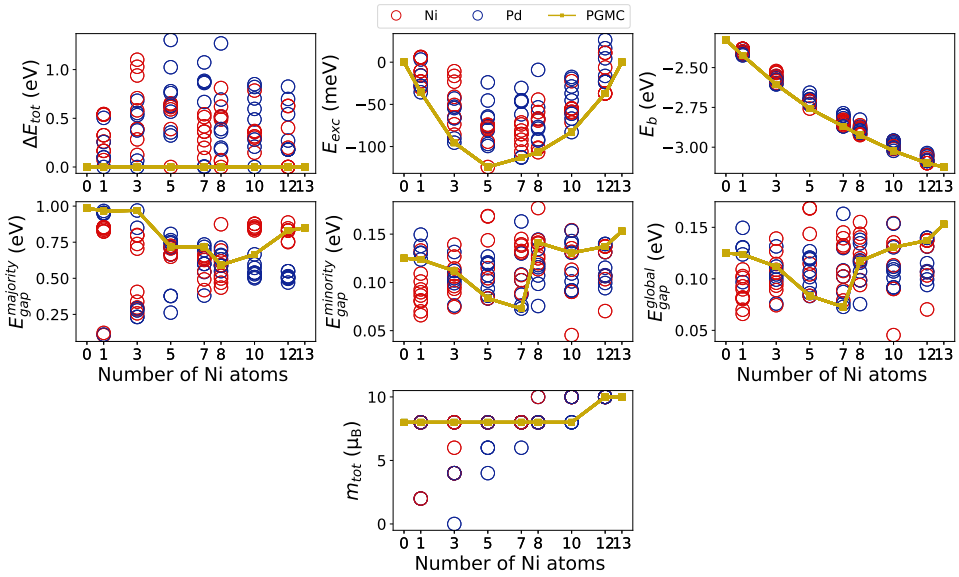

Figure S19: Electronic properties of the Ni_mPd_{13-m} structures. Different colors indicate the starting parent structure. Due to the reduced number of possible permutations at this cluster size, we have generated all possible structures, and thus we do not differentiate between random and designed structures.

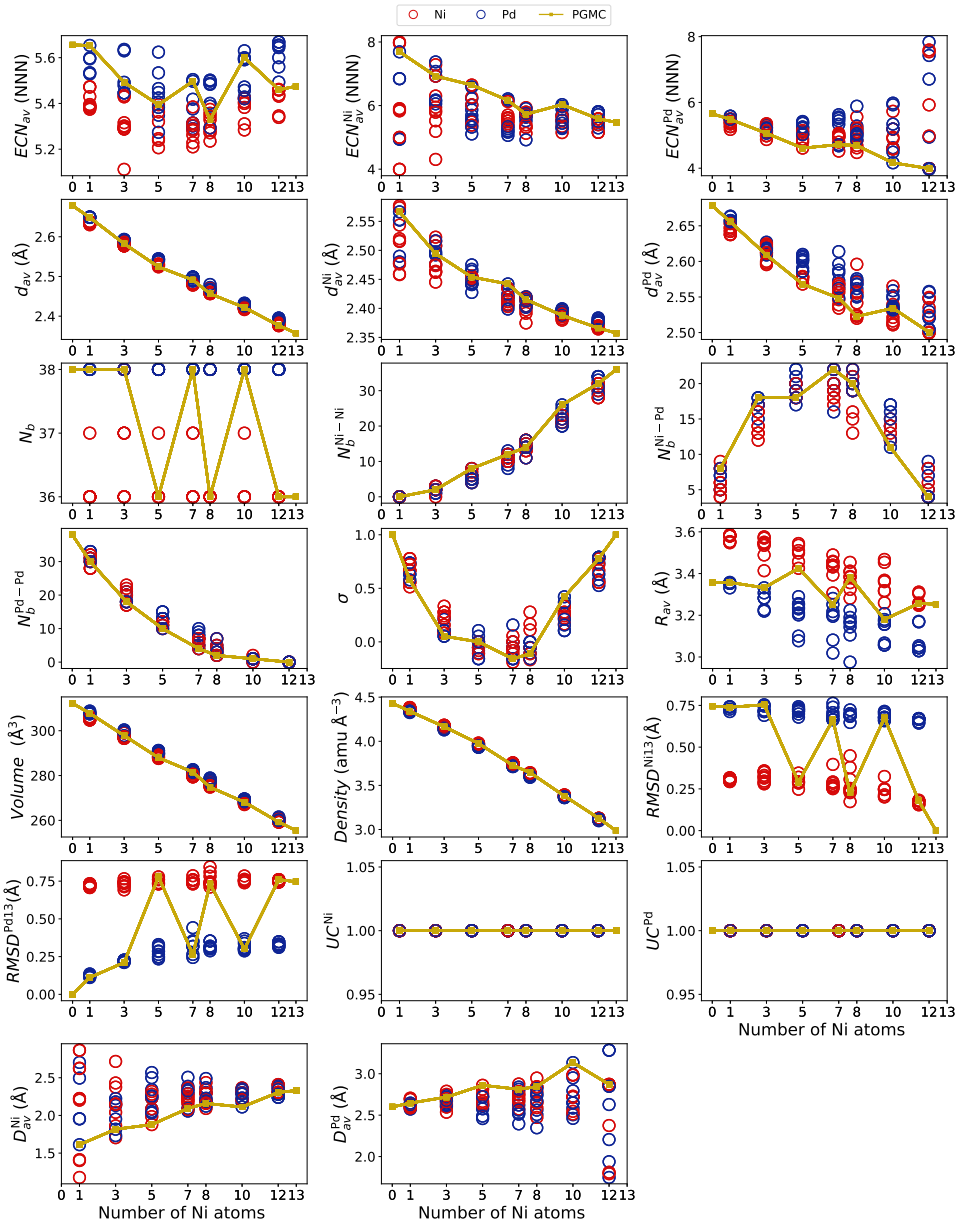

Figure S20: Structural properties of the Ni_mPd_{13-m} structures. Different colors indicate the starting parent structure. Due to the reduced number of possible permutations at this cluster size, we have generated all possible structures, and thus we do not differentiate between random and designed structures.

4.2.2 Final calculations on 27 atom NiPd alloys

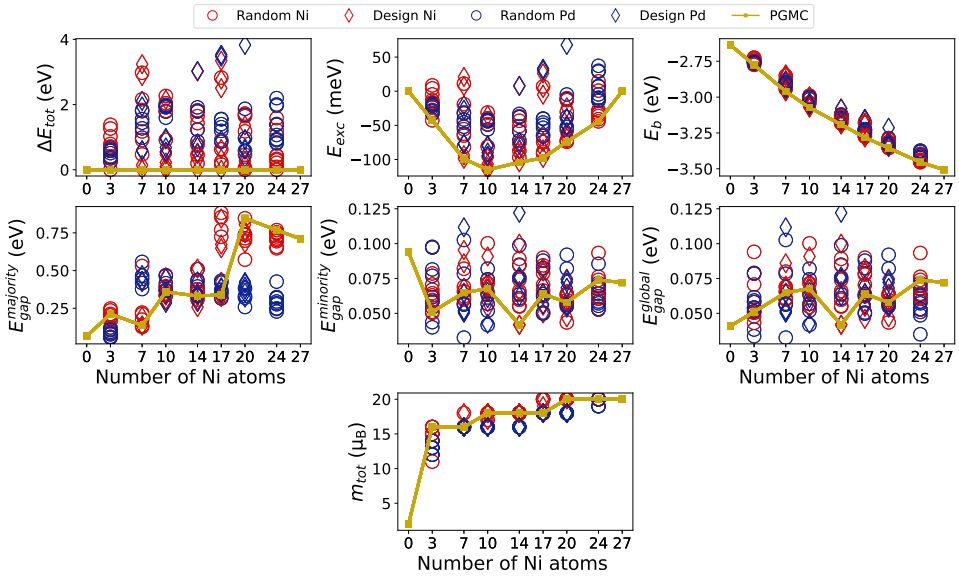

Figure S21: Electronic properties of the Ni_mPd_{27-m} structures. Different colors indicate the starting parent structure, while different symbols differentiate between design-based or random permutations for the generation of the alloys.

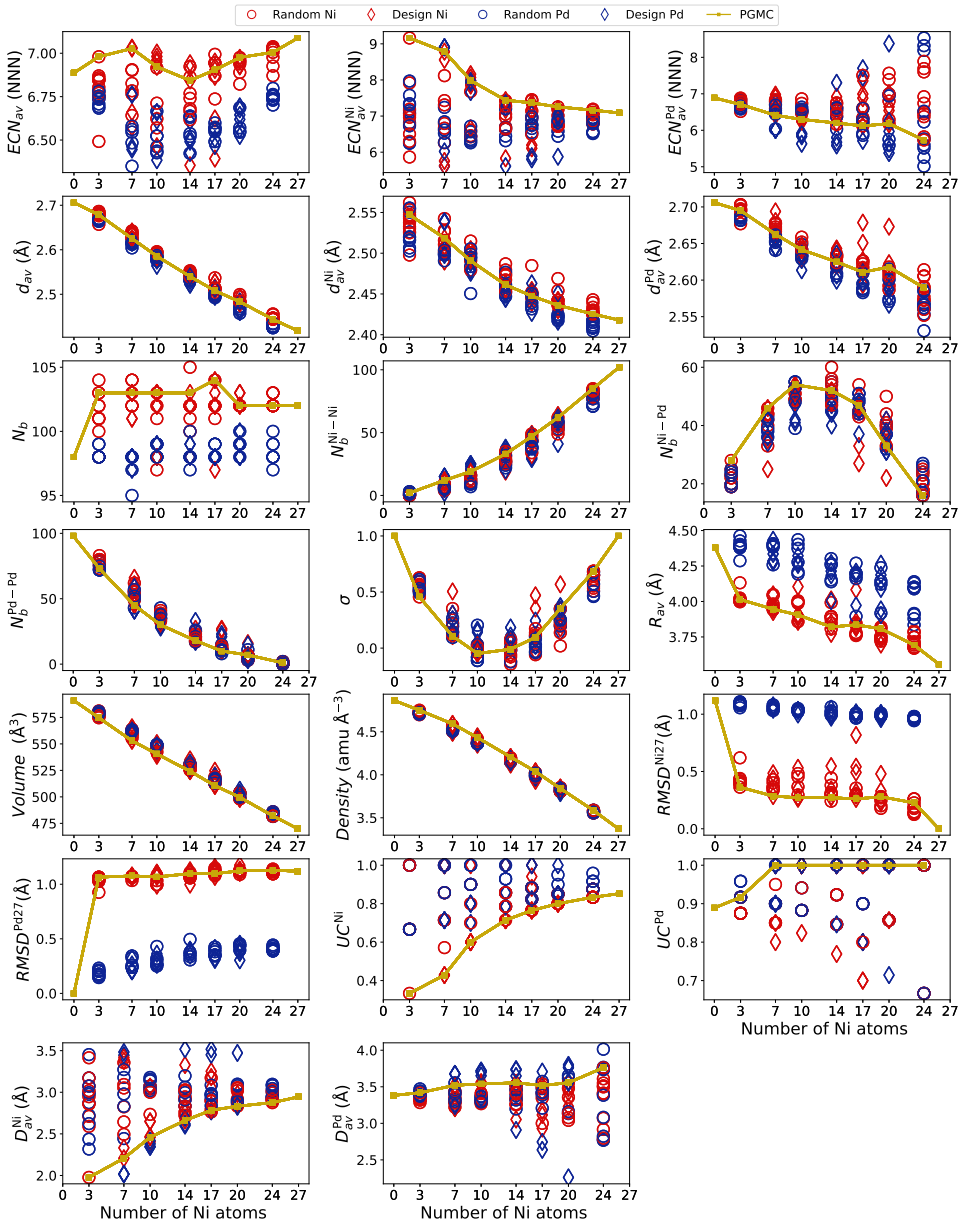

Figure S22: Structural properties of the Ni_mPd_{27-m} structures. Different colors indicate the starting parent structure, while different symbols differentiate between design-based or random permutations for the generation of the alloys.

4.2.3 Final calculations on 41 atom NiPd alloys

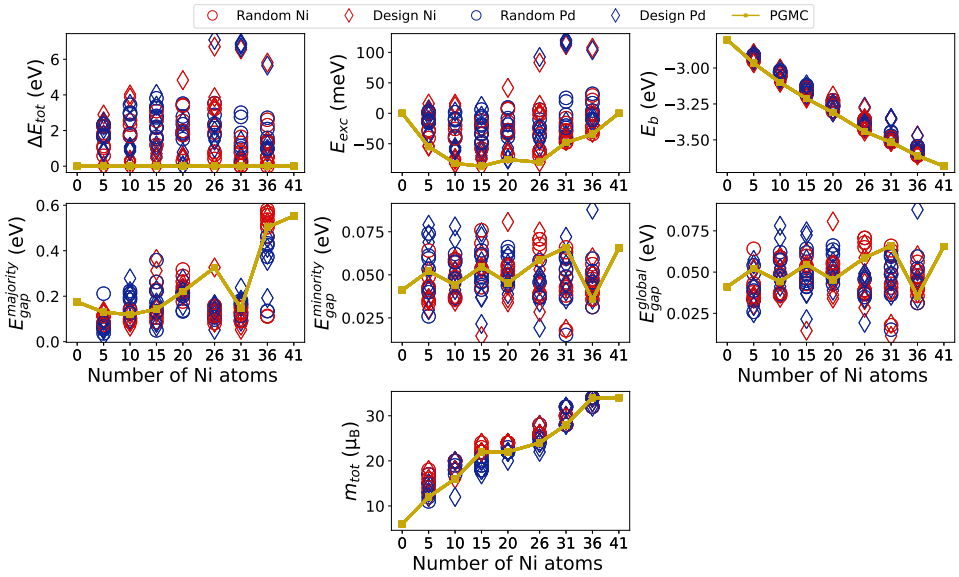

Figure S23: Electronic properties of the Ni_mPd_{41-m} structures. Different colors indicate the starting parent structure, while different symbols differentiate between design-based or random permutations for the generation of the alloys.

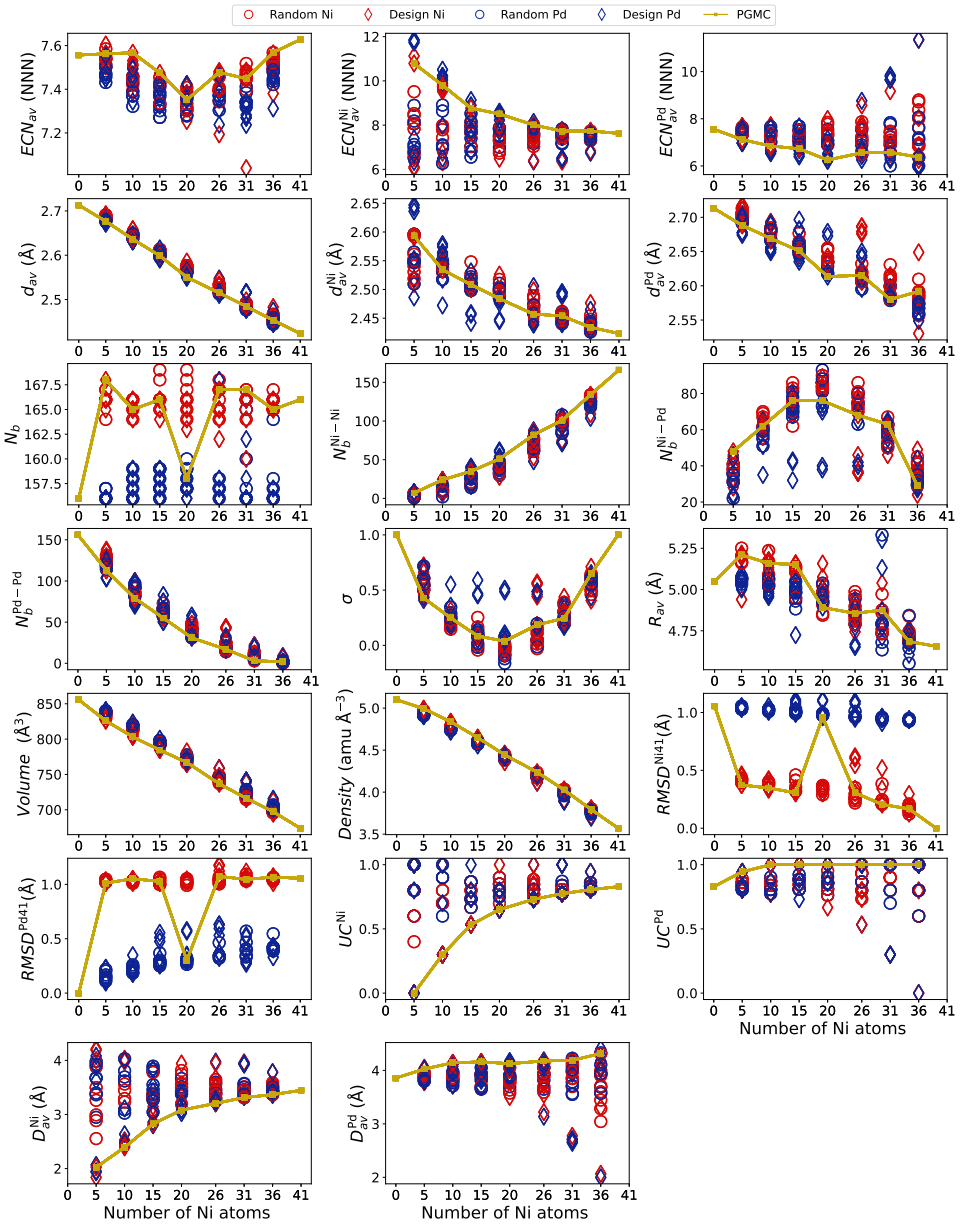

Figure S24: Structural properties of the Ni_mPd_{41-m} structures. Different colors indicate the starting parent structure, while different symbols differentiate between design-based or random permutations for the generation of the alloys.

4.2.4 Spearman correlation

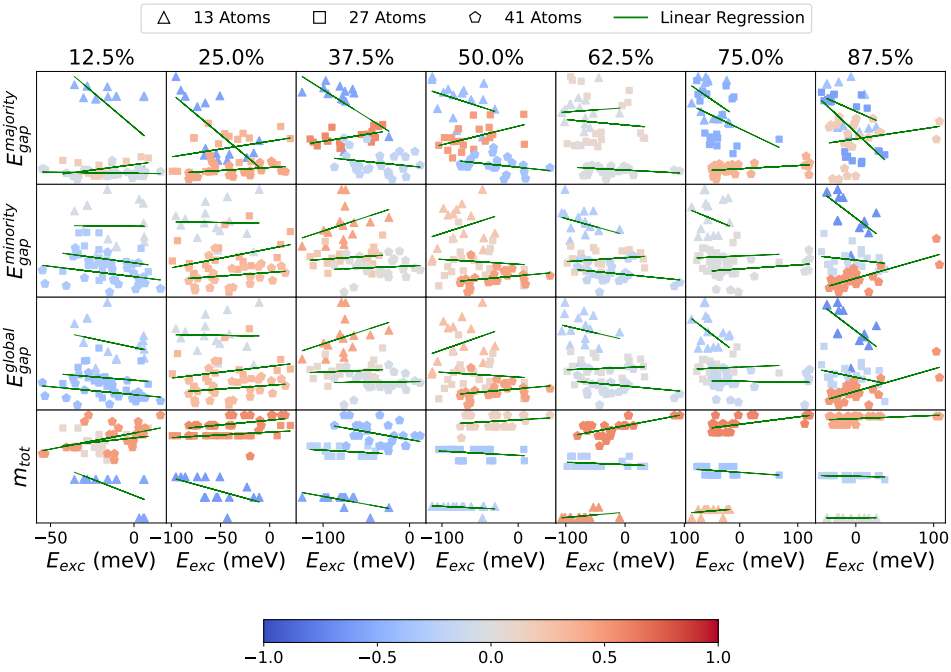

Figure S25: Spearman correlation analysis for electronic and magnetic properties. Each column presents a given percentage of Ni, while the cluster sizes are indicated by different points: Ni_mPd_{13-m} clusters are represented by triangles, Ni_mPd_{27-m} by squares and Ni_mPd_{41-m} by pentagons. The color of the points indicates the value of the correlation coefficient.

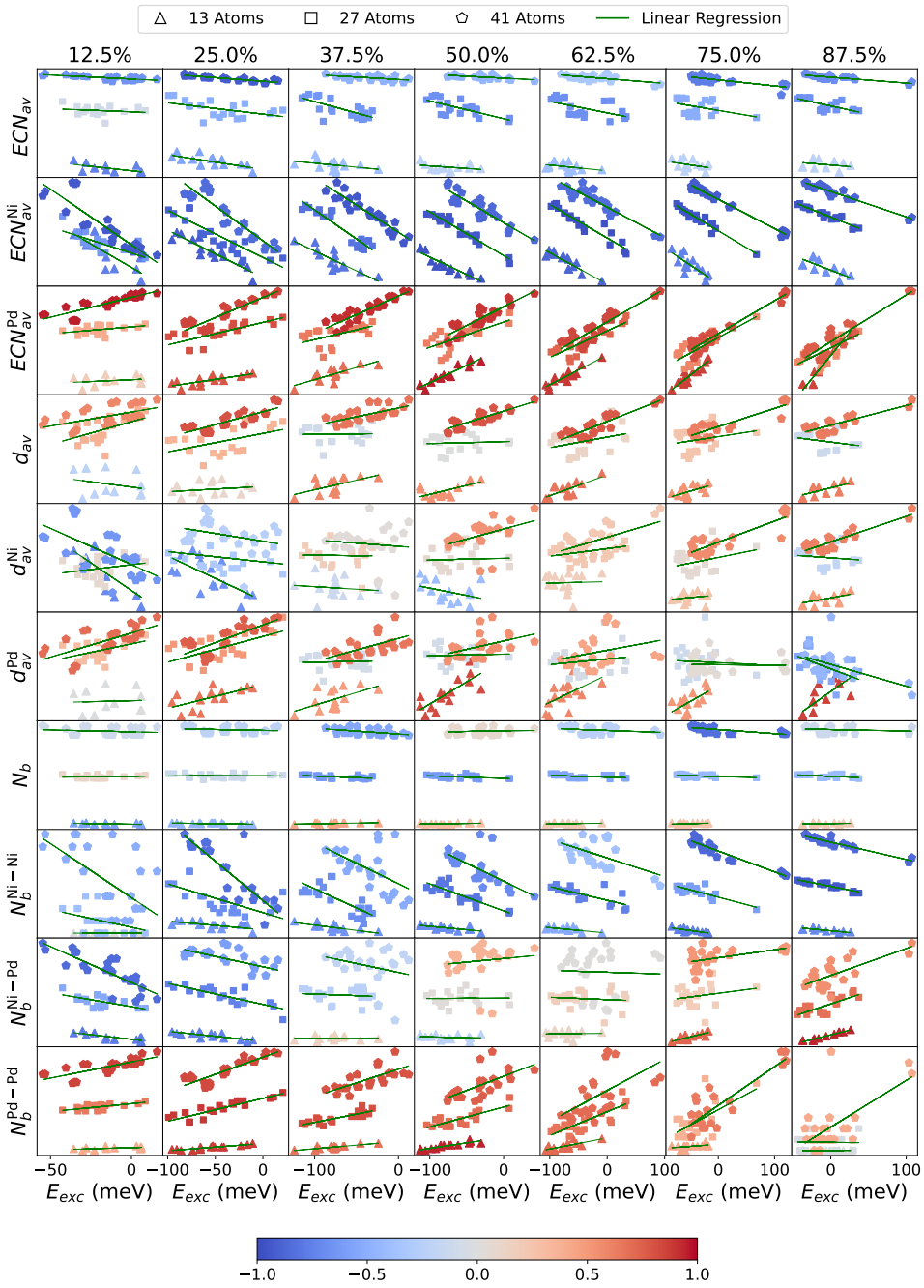

Figure S26: Spearman correlation analysis for structural properties. Each column presents a given percentage of Ni, while the cluster sizes are indicated by different points: Ni_mPd_{13-m} clusters are represented by triangles, Ni_mPd_{27-m} by squares and Ni_mPd_{41-m} by pentagons. The color of the points indicates the value of the correlation coefficient.

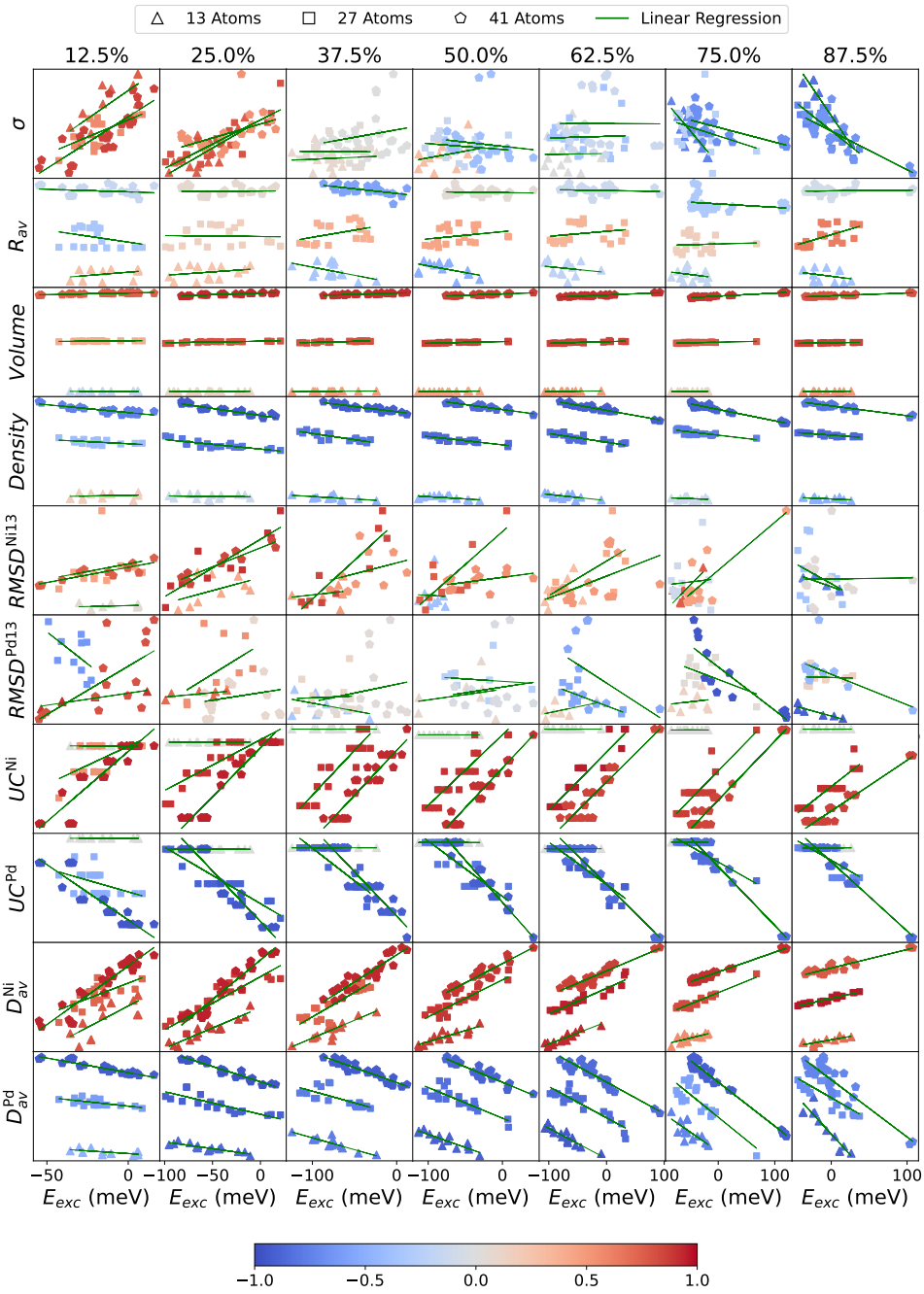

Figure S27: Spearman correlation analysis for structural properties. Each column presents a given percentage of Ni, while the cluster sizes are indicated by different points: Ni_mPd_{13-m} clusters are represented by triangles, Ni_mPd_{27-m} by squares and Ni_mPd_{41-m} by pentagons. The color of the points indicates the value of the correlation coefficient.

References

1 Silva, M. X.; Galvão, B. R. L.; Belchior, J. C. Growth analysis of sodium-potassium alloy clusters from 7 to 55 atoms through a genetic algorithm approach. *J. Mol. Model.* **2014**, *20*, 1–9, DOI: 10.1007/s00894-014-2421-3.

2 Krissinel, E. B.; Jellinek, J. 13-atom Ni – Al alloy clusters: Structures and dynamics. *Int. J. Quantum Chem.* **1997**, *62*, 185–197, DOI: 10.1002/(SICI)1097-461X(1997)62:2.

3 Arslan, H.; Garip, A. K.; Johnston, R. L. Theoretical study of the structures and chemical ordering of cobalt–palladium nanoclusters. *Phys. Chem. Chem. Phys.* **2015**, *17*, 28311–28321, DOI: 10.1039/C5CP01029B.

4 Guedes-Sobrinho, D.; Nomiyama, R. K.; Chaves, A. S.; Piotrowski, M. J.; Da Silva, J. L. F. Structure, Electronic, and Magnetic Properties of Binary Pt_nTM_{55-n} (TM = Fe, Co, Ni, Cu, Zn) Nanoclusters: A Density Functional Theory Investigation. *J. Phys. Chem. C* **2015**, *119*, 15669–15679, DOI: 10.1021/acs.jpcc.5b02242.

5 Batista, K. E. A.; Piotrowski, M. J.; Chaves, A. S.; Da Silva, J. L. F. A Theoretical Investigation of the Structural and Electronic Properties of 55-atom Nanoclusters: The Examples of Y-Tc and Pt. *J. Chem. Phys.* **2016**, *144*, 054310, DOI: 10.1063/1.4941295.

6 Batista, K. E. A.; Da Silva, J. L. F.; Piotrowski, M. J. *Ab initio* Investigation of the Role of Atomic Radius in the Structural Formation of Pt_nTM_{55-n} (TM = Y, Zr, Nb, Mo, and Tc) Nanoclusters. *J. Phys. Chem. C* **2018**, *122*, 7444–7454, DOI: 10.1021/acs.jpcc.7b05714.

7 Batista, K. E. A.; Da Silva, J. L. F.; Piotrowski, M. J. Adsorption of CO, NO and H_2 on the Pd_nAu_{55-n} Nanoclusters: A Density Functional Theory Investigation Within the van der Waals D3 Corrections. *J. Phys. Chem. C* **2019**, *123*, 7431–7439, DOI: 10.1021/acs.jpcc.8b12219.

8 Mendes, P. C. D.; Justo, S. G.; Mucelini, J.; Soares, M. D.; Batista, K. E. A.; Quiles, M. G.; Piotrowski, M. J.; Da Silva, J. L. F. *Ab initio* Insights into the Formation Mechanisms of

55-atom Pt-Based Core-shell Nanoalloys. *J. Phys. Chem. C* **2020**, *124*, 1158–1164, DOI: 10.1021/acs.jpcc.9b09561.

9 Morais, F. O.; Andriani, K. F.; Da Silva, J. L. F. Investigation of the Stability Mechanisms of Eight-atom Binary Metal Clusters Using DFT Calculations and k-means Clustering Algorithm. *J. Chem. Inf. Model.* **2021**, *61*, 3411–3420, DOI: 10.1021/acs.jcim.1c00253.

10 da Silva, L. R.; Morais, F. O.; de Mendonça, J. P. A.; Galvão, B. R. L.; Da Silva, J. L. F. Theoretical investigation of the stability of $A_{55-n}B_n$ nanoalloys (A, B= Al, Cu, Zn, Ag). *Comput. Mater. Sci.* **2022**, *215*, 111805, DOI: 10.1016/j.commatsci.2022.111805.

11 Rupp, M.; Tkatchenko, A.; Müller, K.-R.; von Lilienfeld, O. A. Fast and Accurate Modeling of Molecular Atomization Energies With Machine Learning. *Phys. Rev. Lett.* **2012**, *108*, 058301, DOI: 10.1103/physrevlett.108.058301.

12 Rodriguez, M. Z.; Comin, C. H.; Casanova, D.; Bruno, O. M.; Amancio, D. R.; Costa, L. d. F.; Rodrigues, F. A. Clustering algorithms: A comparative approach. *PloS one* **2019**, *14*, e0210236, DOI: 10.1371/journal.pone.0210236.

13 vd Maaten, L.; Hinton, G. Visualizing data using t-sne. *J. Mach. Learn. Res.* **2008**, *9*, 2579–2605.

14 Lu, Q. L.; Luo, Q. Q.; Chen, L. L.; Wan, J. G. Structural and Magnetic Properties of $Ni_n(n = 2-21)$ Clusters. *Eur. Phys. J. D* **2011**, *61*, 389–396, DOI: 10.1140/epjd/e2010-10129-8.

15 Chaves, A. S.; Piotrowski, M. J.; Da Silva, J. L. F. Evolution of the Structural, Energetic, and Electronic Properties of the 3*d*, 4*d*, and 5*d* Transition-metal Clusters (30 TM_n Systems for $n = 2-15$): A Density Functional Theory Investigation. *Phys. Chem. Chem. Phys.* **2017**, *19*, 15484–15502, DOI: 10.1039/c7cp02240a.

16 Montejano-Carrizales, J. M.; Iniguez, M. P.; Alonso, J. A.; López, M. J. Theoretical Study of Icosahedral Ni Clusters within the Embedded-Atom Method. *Phys. Rev. B* **1996**, *54*, 5961, DOI: 10.1103/PhysRevB.54.5961.

17 Lathiotakis, N. N.; Andriotis, A. N.; Menon, M.; Connolly, J. Tight Binding Molecular Dynamics Study of Ni Clusters. *J. Chem. Phys.* **1996**, *104*, 992–1003, DOI: 10.1063/1.470823.

18 Nayak, S. K.; Khanna, S. N.; Rao, B. K.; Jena, P. Physics of Nickel Clusters: Energetics and Equilibrium Geometries. *J. Phys. Chem. A* **1997**, *101*, 1072–1080, DOI: 10.1021/jp962720r.

19 Grigoryan, V. G.; Springborg, M. A Theoretical Study of the Structure of Ni Clusters (Ni_N). *Phys. Chem. Chem. Phys.* **2001**, *3*, 5135–5139, DOI: 10.1039/B105831M.

20 Doye, J. P. K.; Wales, D. J. Global Minima for Transition Metal Clusters Described by Sutton–Chen Potentials. *New J. Chem.* **2018**, *22*, 733–744, DOI: 10.1039/A709249K.

21 Blanco-Rey, M.; Juaristi, J. I.; Alducin, M.; López, M. J.; Alonso, J. A. Is spillover relevant for hydrogen adsorption and storage in porous carbons doped with palladium nanoparticles? *The Journal of Physical Chemistry C* **2016**, *120*, 17357–17364, DOI: 10.1021/acs.jpcc.6b04006.

22 Nava, P.; Sierka, M.; Ahlrichs, R. Density Functional Study of Palladium Clusters. *Phys. Chem. Chem. Phys.* **2003**, *5*, 3372–3381, DOI: 10.1039/b303347c.

23 López, M. J.; Jellinek, J. Fragmentation of Atomic Clusters: A Theoretical Study. *Phys. Rev. A* **1994**, *50*, 1445, DOI: 10.1103/PhysRevA.50.1445.

24 Sachdev, A.; Masel, R. I.; Adams, J. B. An embedded atom method study of the equilibrium shapes of small platinum and palladium clusters. *Z. Phys. D: At., Mol. Clusters* **1993**, *26*, 310–312, DOI: 10.1007/BF01429178.

25 Grigoryan, V. G.; Springborg, M. Structural and Energetic Properties of Nickel Clusters: $2 < N < 150$. *Phys. Rev. B* **2004**, *70*, 205415, DOI: 10.1103/physrevb.70.205415.

26 Xing, X.; Hermann, A.; Kuang, X.; Ju, M.; Lu, C.; Jin, Y.; Xia, X.; Maroulis, G. Insights into the geometries, electronic and magnetic properties of neutral and charged palladium clusters. *Sci. Rep.* **2016**, *6*, 1–11, DOI: 10.1038/srep19656.

27 Piotrowski, M. J.; Ungureanu, C. G.; Tereshchuk, P.; Batista, K. E. A.; Chaves, A. S.; Guedes-Sobrinho, D.; Da Silva, J. L. F. Theoretical Study of the Structural, Energetic, and Electronic Properties of 55-atom Metal Nanoclusters: A DFT Investigation Within van der Waals Corrections, Spin-orbit Coupling, and PBE+U of 42 Metal Systems. *J. Phys. Chem. C* **2016**, *120*, 28844–28856, DOI: 10.1021/acs.jpcc.6b10404.